remote sensing

MDPI

Article

Measurements of Rainfall Rate, Drop Size Distribution, and Variability at Middle and Higher Latitudes: Application to the Combined DPR-GMI Algorithm

Viswanathan Bringi [1,*], Mircea Grecu [2], Alain Protat [3], Merhala Thurai [1] and Christian Klepp [4]

[1] Department of Electrical and Computer Engineering, Colorado State University, Fort Collins, CO 80523, USA; merhala@engr.colostate.edu
[2] Laboratory for Atmospheres and NASA GSFC, Morgan State University, Baltimore, MD 21251, USA; mircea.grecu-1@nasa.gov
[3] Australian Bureau of Meteorology, Melbourne, VIC 3001, Australia; alain.protat@bom.gov.au
[4] Max Planck Institute for Meteorology, 20146 Hamburg, Germany; christian.klepp@mpimet.mpg.de
* Correspondence: bringi@engr.colostate.edu; Tel.: +1-970-491-7678

Abstract: The Global Precipitation Measurement mission is a major U.S.–Japan joint mission to understand the physics of the Earth's global precipitation as a key component of its weather, climate, and hydrological systems. The core satellite carries a dual-precipitation radar and an advanced microwave imager which provide measurements to retrieve the drop size distribution (DSD) and rain rates using a Combined Radar-Radiometer Algorithm (CORRA). Our objective is to validate key assumptions and parameterizations in CORRA and enable improved estimation of precipitation products, especially in the middle-to-higher latitudes in both hemispheres. The DSD parameters and statistical relationships between DSD parameters and radar measurements are a central part of the rainfall retrieval algorithm, which is complicated by regimes where DSD measurements are abysmally sparse (over the open ocean). In view of this, we have assembled optical disdrometer datasets gathered by research vessels, ground stations, and aircrafts to simulate radar observables and validate the scattering lookup tables used in CORRA. The joint use of all DSD datasets spans a large range of drop concentrations and characteristic drop diameters. The scaling normalization of DSDs defines an intercept parameter N_W, which normalizes the concentrations, and a scaling diameter D_m, which compresses or stretches the diameter coordinate axis. A major finding of this study is that a single relationship between N_W and D_m, on average, unifies all datasets included, from stratocumulus to heavier rainfall regimes. A comparison with the N_W–D_m relation used as a constraint in versions 6 and 7 of CORRA highlights the scope for improvement of rainfall retrievals for small drops (D_m < 1 mm) and large drops (D_m > 2 mm). The normalized specific attenuation–reflectivity relationships used in the combined algorithm are also found to match well the equivalent relationships derived using DSDs from the three datasets, suggesting that the currently assumed lookup tables are not a major source of uncertainty in the combined algorithm rainfall estimates.

Keywords: raindrop size distributions; GPM-DPR-combined algorithms; scattering at Ku and Ka-bands

Citation: Bringi, V.; Grecu, M.; Protat, A.; Thurai, M.; Klepp, C. Measurements of Rainfall Rate, Drop Size Distribution, and Variability at Middle and Higher Latitudes: Application to the Combined DPR-GMI Algorithm. *Remote Sens.* **2021**, *13*, 2412. https://doi.org/10.3390/rs13122412

Academic Editors: Christopher Kidd and Lisa Milani

Received: 19 May 2021
Accepted: 17 June 2021
Published: 20 June 2021

1. Introduction

Two of the main instruments onboard the Global Precipitation Measurement (GPM) satellite are the Dual Precipitation Radar (DPR) and the GPM-Microwave-Imager (GMI). The retrieval algorithms for DPR and combined DPR-GMI (referred in the abstract as CORRA, (henceforth referred to as the Combined Algorithm or CMB) have adopted the scaled-normalized drop size distribution (hereafter referred to as the DSD) formulation of Testud et al., Bringi et al., and Lee et al. [1–3], respectively, as the basis for the rainfall retrieval procedure. The advantage, as pointed out numerous times in the literature, is that

the process of scaling and normalizing the N(D) by two reference moments [4] reveals the 'underlying' or intrinsic shape of the DSD with highly compressed scatter as compared to using the un-normalized gamma popularized by Ulbrich [5]. The normalized DSD can be written in compact form as $N(D) = N_0' h(x)$ where N_0' is the 'normalized' intercept parameter and $x = D/D_m$, where D_m is the ratio of the fourth to third reference moments of the DSD [1]. The N_0' is the intercept parameter of an exponential DSD, which has the same D_m and rain water content as the actual distribution.

Recent observations of the DSD using collocated high resolution optical array probe (known as the Meteorological Particle Spectrometer or MPS); [6]) for drizzle and small drops (D < 1 mm) and 2D-video disdrometer (2DVD; [7,8]) for larger drops (>0.75 mm) have shown that normalizing N(D) by N_W and scaling D by D_m leads to the generalized gamma model as a good "climatological" fit for h(x) describable by two shape parameters (μ_{GG}, c) [9]. The GPM-dual-precipitation radar (or DPR) and CMB algorithms currently use the legacy standard gamma model for h(x) with one shape parameter, μ, fixed at 2 or 3, which gives a convex down shape for a small x (<0.5) relative to the concave up shape for the generalized gamma [10]. This is due to small drop truncation (e.g., due to poor sensitivity and/or resolution or other problems; [11]) exhibited by the legacy Joss disdrometers [12] used during the earlier Tropical Measurement Mission (TRMM).

Small drop truncation strongly affects the lower order moments (0–2) of the DSD and related microphysical processes, such as total number density, evaporation, gravitational sedimentation, etc. Higher order moments of 3 and higher, for example N_W, defined (to within a constant) by the ratio M_3/D_m^4, where $D_m = M_4/M_3$, are less affected. In particular, the accurate retrieval of N_W with low bias (or, low systematic error) has proven to be difficult for the CMB algorithm due to its high variability spanning nearly three orders of magnitude [13].

The GPM-DPR and CMB algorithms have been deemed as having met the level II error requirement (both systematic and random) for both D_m and R of 25% for $D_m > 0.5$ mm [14], but no such requirement has been placed on N_W, mainly due to its large variability. The difficulty in estimating N_W with low systematic error even with powerful algorithms based on optimal estimation or ensemble filtering [15] perhaps lies in not having sufficient data to accurately formulate the error covariance matrix of the a priori state suitable for the climatology under consideration. Of course, there are other sources of error that are not well understood or can be modeled accurately enough (Non-Uniform Beam Filling (NUBF) correction, multiple scattering, ice scattering, etc.). Our goal in this article is more modest and limited to the improvement of the CMB algorithm by using measured DSDs at the middle and upper latitudes, where the benchmark (monthly) latitudinal average using the Integrated Multi-satellitE Retrievals for GPM (IMERG) [16] is systematically higher than the CMB by as much as 100% [17]. It should be noted, however, that the limited sensitivity of the DPR is a major factor contributing to the disagreement between the CMB and IMERG estimates. The main caveat in our study is that disdrometer data are collected at the surface (overland or ocean) with poor spatial sampling [18] and reliance has to be placed on vertical pointing Doppler radars (e.g., Micro rain radar, MRR) or the operational radar networks (e.g., WSR-88D system), which are considered 'secondary' because there is no direct estimator of N_W that can be validated.

In the current version (V6) of the CMB, the D_m is not included in the state vector; rather, it is tied to the Ku-band radar reflectivity (Z_e) profile and a generalized Hitschfeld-Bordan (H-B; [19]) attenuation correction methodology [15]. Whereas the N_W parameter is set a priori at five different altitudes with assumed spatial correlation based on numerical modeling [15] and other ground-validation (GV) radar estimation of the same [20], the mean a priori values of N_W in rain of 15,660 mm^{-1} m^{-3} for convective and 7420 for stratiform rain [21], which largely reflects the TRMM legacy and could be significantly biased in the mid-upper latitude N and S hemispheres as shown by Protat et al. [22,23] and Duncan et al. [24]. Given the large variability of N_W and uncertainty of accuracy in light rainfall, a new CMB formulation was recently implemented [25] to better account for

the inverse relation between N_W and D_m, which has been verified in numerous GPM-GV field programs [26,27]. In the new formulation, D_m is first estimated without accounting for the relation between N_W and D_m, and, in a second step, N_W is nudged towards an N_W–D_m climatological relationship. Retrieval of the parameter, mainly N_W, using the state-of-the-art NASA GPM-GV polarimetric radar, is not entirely satisfactory [28].

In view of these recent CMB algorithmic developments, our main goal in this study is to compare the statistical properties of DSD parameters and statistical relationships between radar observables and DSD parameters using our measured DSDs with assumptions currently held in the CMB algorithm. The focus of our study is on characterizing such properties in order to complement recent studies where such properties and relationships have been derived for a variety of other different rain types [22,23,27,29].

Here, we investigate unconditionally and jointly two main DSD parameters (the normalized intercept N_W and the mass-weighted mean diameter D_m) of rain drop size distributions from three different rain regimes (a fourth separate regime is the outer rain bands of organized oceanic systems after landfall). Our motivation is driven by the need to better understand and mitigate uncertainties in the GPM radar–radiometer precipitation combined algorithm.

This paper is organized as follows: Section 2 describes the DSD datasets collected by various instruments in different locations and climates. Section 3 describes the data analysis procedures and results, including the statistical relationships between DSD parameters as well as scattering simulations of radar reflectivities and specific attenuations at ku and ka bands. These are compared with the lookup tables used by the CMB algorithm, which are based on the normalized gamma DSD model. Section 4 focuses on the correlation between N_W and D_m and provides a discussion on the nudging of N_W and its impact on the retrievals. We conclude with a discussion of our results and summarize the key points in Section 5.

2. Instrumentation and Data Collection

Below is a brief summary of the measured DSD sets included in this study (and DSDs from simulated gamma with uncorrelated parameters):

(a) Measured DSDs from semi-arid Greeley (GXY), Colorado, USA, and sub-tropical Huntsville (HSV), Alabama, USA, are collated together to form about 2928 3-min averaged DSDs. At each site the 2DVD and MPS instruments were placed inside a 2/3-scaled DFIR (Double Fence Intercomparison Reference windshield [30]). An identical instrument suite was recently installed at the Wallops Precipitation Research Facility (henceforth WFF), to represent a mid-latitude coastal location. Since all three sites had identical instruments, the comparison between them would not have the uncertainty and other complications of using different sensors. The data quality procedures typically follow Schoenhuber et al. [7,8], with some caveats noted by [31].

(b) The NCAR C-130 was operated off the coast of Chile [32] equipped with a 'fast' 1-s 2D-C probe in stratocumulus drizzle (warm rain). The total number of 1-s DSDs was 4142, all quality controlled (J. Jensen, NCAR, personal communication).

(c) A very large (arguably the largest ever quality controlled) set of DSDs acquired over the open ocean (OceanRain) described by Klepp et al. [33] and Protat et al. [22,23].

(d) Simulations of gamma DSDs with uncorrelated N_W, D_m, and shape parameter (μ).

(e) The outer rain bands of: (a) Category-1 Hurricane Dorian, described by Thurai et al. [34] and modeled using a cloud particle model by Bringi et al. [35], which traversed the WFF disdrometer network site for ≈8 h; (b) tropical storm Irma (<14 h) near the Huntsville site; (c) tropical depression Nate, which was very shallow at times with negligible echo above the melting layer and 'pure' warm rain at times (overall <16 h) near Huntsville. Figure 1 shows the locations marked as WFF and HSV. The outer rainbands were typically stratiform in nature and occurred in the down shear left quadrant. The reason for including these DSDs is because the dynamics

are known to be very different from the stratiform rain produced by mesoscale convective complexes.

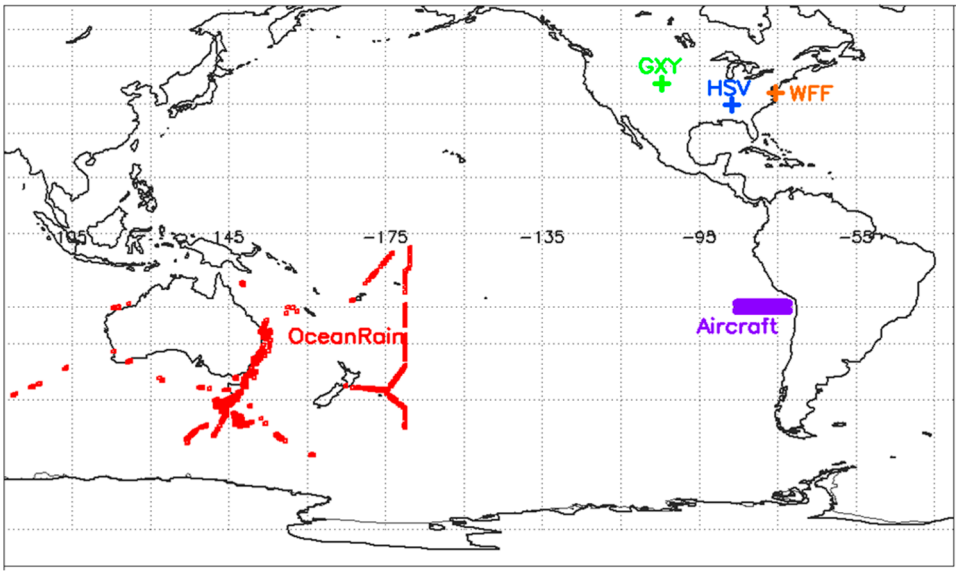

Figure 1. Locations of sites where MPS and 2DVD were deployed for Ground Validation. The purple rectangle depicts the region penetrated by the C-130. The red lines depict the tracks of the R/V Investigator in 2016 and 2018.

A global location map of the regions where data (a–c) were collected is depicted in Figure 1, and Table 1 gives some brief information relating to the type of instruments, references to the data quality, and other salient features. As can be easily seen in Figure 1, the OceanRain project with an ODM-470 optical disdrometer 'hardened' for shipborne deployment (sited on top of the mast, with a wind vane to orient the instrument perpendicular to the main flow) has the largest number of 1-min DSD data collected during the voyages of the Australian Research Vessel Investigator from 2016 to 2018 covering the middle-to-upper latitudes of the S hemisphere.

Table 1. Brief summary of the ground-based/OceanRain and C-130 instrumentation.

Dataset	Instruments	Number of DSDs	Location
Ground-based (green, blue, and orange '+' marks in Figure 1)	i. Meteorological Particle Spectrometer (MPS) ii. 2D Video Disdrometer (2DVD)	A total of 2928 3-min 'complete' DSDs	Three fixed locations i. Greeley, Colorado (six months in Spring-summer in 2015 under the CSU-CHILL radar coverage (Bringi et al. 2020) ii. Huntsville, Alabama (2016–current) iii. Wallops, Virginia (installed on 1 August 2019)
C-130 penetrations in stratocumulus drizzle off the coast of Chile (purple area in Figure 1)	'fast' 2D-cloud probe (25 micron resolution)	1-s data: 4412 DSDs	1.4 km altitude, off the coast of Chile in stratocumulus drizzle.
Open ocean (shown as red squares in Figure 1)	ODM 470 optical disdrometer	1-min DSDs: 14,213	Ocean regions surrounding Australia plus south-west Pacific.
Outer rain bands * (blue and orange '+' marks in Figure 1)	i. MPS ii. 2DVD	A total of 1403 3-min 'complete' DSDs	Two fixed locations i. Huntsville, Alabama ii. Wallops, Virginia

* Tropical Depression Nate over HSV, Tropical Depression Irma over HSV and category 1 Hurricane over WFF.

3. Data Analysis

3.1. The 'Intrinsic' DSD Shape: Marine Stratocumulus Drizzle versus Semi-Arid and Sub-Tropical Regimes

We followed the methodology of Lee et al. [3] for the normalization of the DSDs. The reference moments chosen here are M_3 and M_4. Recall that h(x) is defined via $N(D) = N_0' h(x)$, where $x = D/D_m$. The functional form of h(x) does not necessarily have to be specified as long as its moments are finite. A flexible form used by Thurai and Bringi [9], Protat et al. [22], and Duncan et al. [24] is the generalized gamma, which has two shape parameters. The N_0' is termed the 'normalized' intercept parameter and D_m, defined as M_4/M_3, is termed the mass-weighted mean diameter.

Figure 2 shows the double-moment normalization [3] applied to the combined Greeley (GXY) and Huntsville (HSV) datasets (scatter plot depicted as black-filled circle markers). The color contours depict the 2D histogram or density plot of h(x) using the 4412 1-s stratocumulus drizzle DSDs. The color bar shows the contours of log N. The maximum D_m of the drizzle DSDs was about 0.5 mm (see Figure 3a later). Hence, to compare the h(x) between the drizzle and the GXY-HSV data, we chose to threshold the latter at $D_m = 0.5$ mm for consistency.

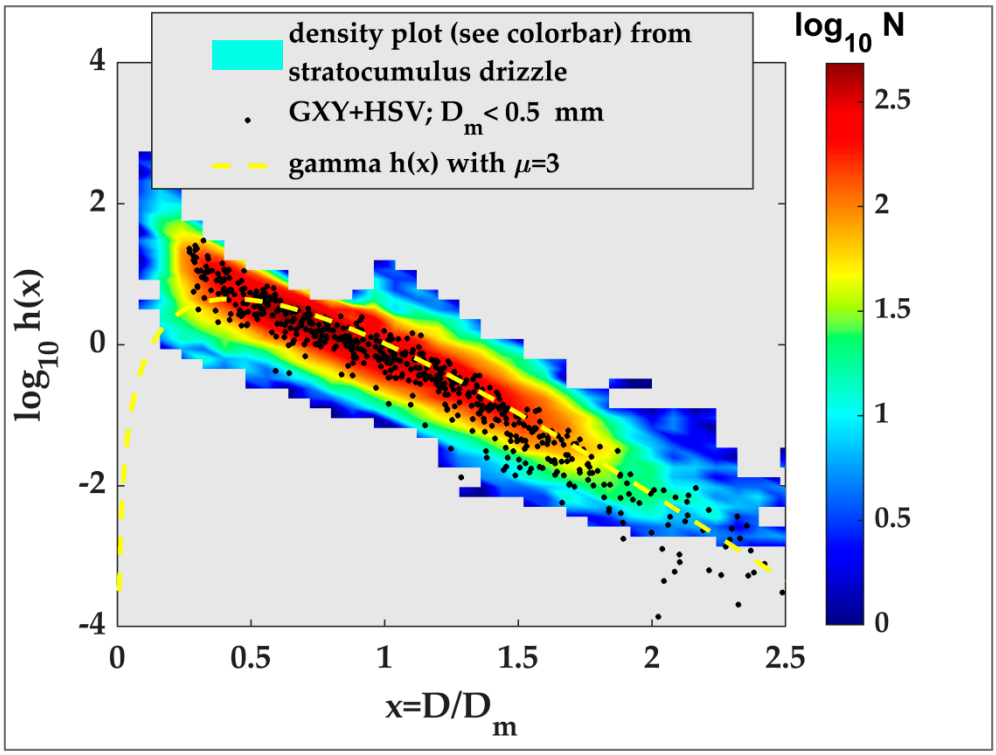

Figure 2. Density plot of h(x) from stratocumulus drizzle with number of occurrences given by the color bar in contours of log N. The GXY-HSV data are pooled together for $D_m < 0.5$ mm and shown as black points. The dashed yellow line is the h(x) for the gamma model with $\mu = 3$.

The colored contours of the density of h(x) for the drizzle are compact and the scatter of the GXY-HSV h(x) are noted to be well-confined by the contour at N = 100, which is indicative of h(x) stability across very different rainfall regimes, e.g., [9,22]. Also shown in Figure 2 is the h(x) for the gamma model with $\mu = 3$. The agreement is quite good for $x > 0.5$, below which the h(x) drops off very rapidly, whereas when two disdrometers are used, such as MPS and 2DVD, the $x < 0.5$ region is shaped concave up (as in [36]). The total drop concentration in the gamma model with $\mu = 2$ to 3 can be low by an order of magnitude, which will bias, for example, the rain water content and the Ka-band specific attenuation, which are linearly related (we are referring to below cloud base, thus excluding

cloud droplets). This is bound to impact the CMB algorithm, where the Ka-band reflectivity and path integrated attenuation are simulated from the attenuation-corrected Ku-band radar data.

3.2. Histograms of DSD Parameters

The histograms of the DSD parameters [$\log_{10}$ (N_W); D_m] give valuable information when different rain regimes are compared. Note that these parameters can be computed for any measured DSD. Figure 3 panel (a) shows the histogram of D_m and panel (c) shows $\log_{10}$ N_W from stratocumulus drizzle using a 'fast' 2D-cloud probe (on aircraft) with a 25 μm resolution. The shape o latter is quite symmetric about the mode which is high at 10^6 mm^{-1} m^{-3}. The aircraft also had a cloud droplet probe (CDP) to measure in-cloud size spectra. The stratocumulus clouds were warm, and both cloud droplets and drizzle were present. However, the size spectra from the 2D-C probe, when compared with the droplet spectra from the CDP, showed spectral separation at sizes of about 50 μm. Hence, we have no reason to believe that the $\log_{10}$ N_W histogram of drizzle in panel (c) is incorrect. The D_m histogram of drizzle in panel (a) is very positively skewed and of unusual shape.

Panels (b) and (c) of Figure 3 compare the histograms of D_m and log N_W from overland and over ocean. The differences in the shape, mode, and width indicate that oceanic DSDs from the Southern Hemisphere high latitudes are characterized by lower concentrations of slightly bigger drops than DSDs over land. The difference in log (N_w) is consistent with the latitudinal variability observed between oceanic DSDs from the Southern Hemisphere high-latitude and from the Northern Hemisphere mid-latitude bands discussed in [22]. However, no difference was observed between the oceanic D_m in those two latitude bands. Therefore, the observed variability between the two datasets seems to be attributable to a mixture of latitudinal and land versus ocean variability.

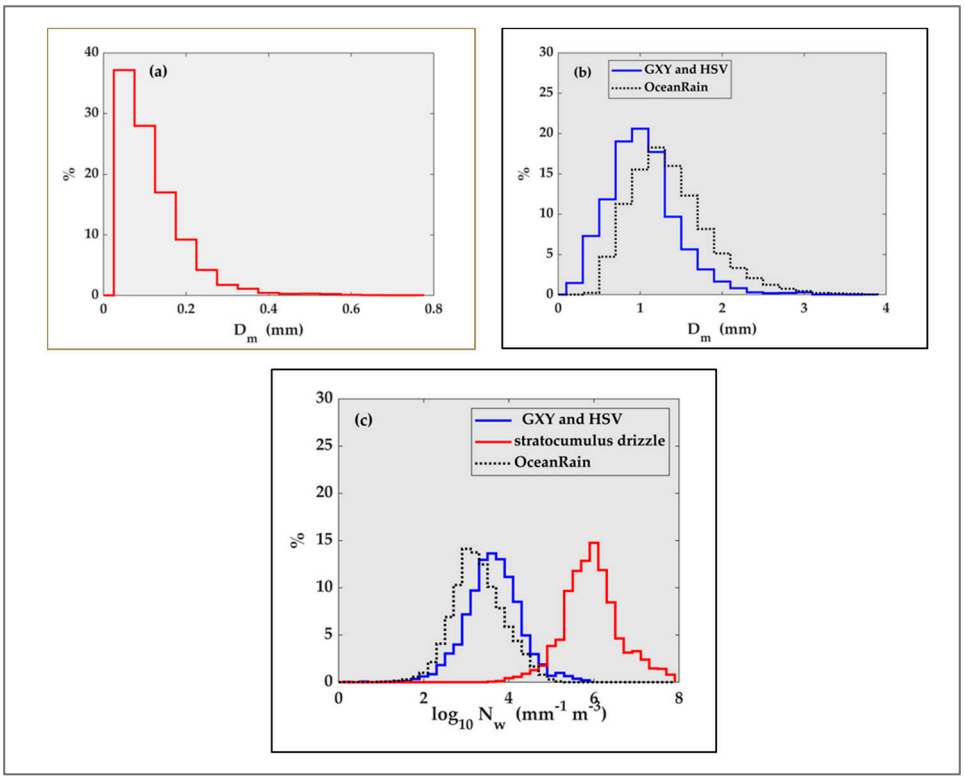

Figure 3. Relative frequency histograms of (**a**) D_m from stratocumulus drizzle, (**b**) same as (**a**) but from OceanRain and pooled DSDs from GXY-HSV, and (**c**) histograms of $\log_{10}$ (N_W) from OceanRain and pooled DSDs and from stratocumulus drizzle (red line).

Liao et al. [29] obtained histogram shapes and modal values very close to our GXY-HSV combined histogram. Their database had >216,000 1-min DSDs using Parsivel disdrometers from NASA Ground Validation field projects such as MC3E, IFLOODs, and Wallops, representing regimes corresponding to deep summer convection in central Oklahoma, springtime convection in Iowa, and mid-latitude coastal regimes, respectively.

It is clear that marine drizzle cannot be detected by the Ku- or Ka-band radars. However, the plot of Z_{ku} versus D_m (see Figure 4) from drizzle and GXY-HSV illustrates that perhaps the drizzle branch 'joins' the more intense rainfall region fairly continuously. The reflectivity of drizzle at Ku-band varies very sharply as D_m increases (the drizzle is shown as a density plot) like a nearly 'vertical' tower, with D_m approximately constant at around 0.2 mm, while N_W increases with Z_{ku}. This feature of very tight compression generally occurs only when Z_{ku} is normalized by N_W prior to plotting against D_m. The scatter plot in Figure 4 is from GXY-HSV, which shows that increasing Z_{ku} is accompanied by increasing D_m, along with much higher variability.

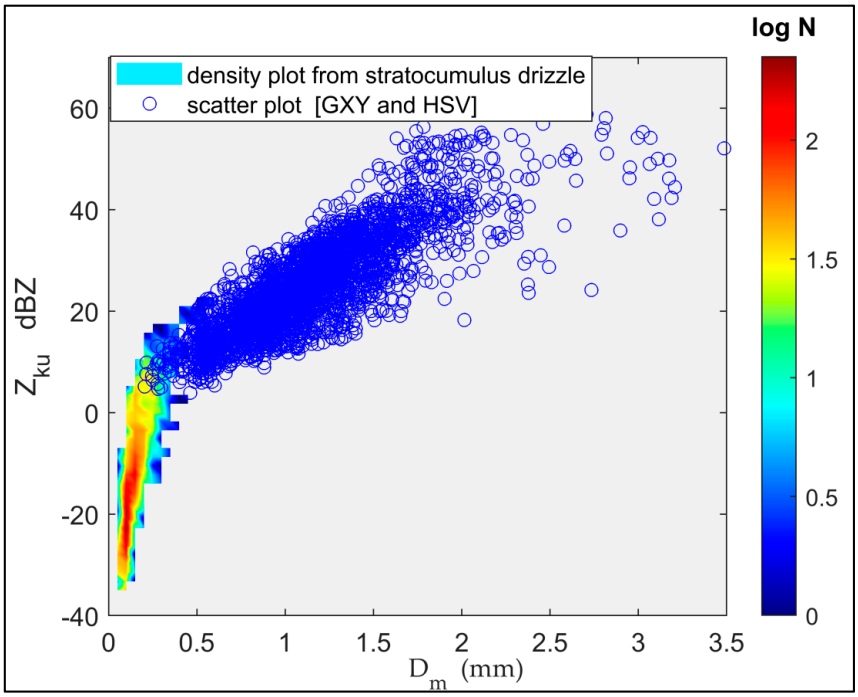

Figure 4. Scatterplot of the reflectivity at the Ku-band versus D_m from stratocumulus drizzle (density-plot in color) and from all DSDs from GXY-HSV (blue points).

3.3. N_W versus D_m

As discussed previously, the most important covariability (next to D_m versus R) of the DSD gamma parameters used in the CMB algorithm is between $\log(N_W)$ and D_m, which enables one to choose the a priori state as well as to nudge the $\log(N_W)$ in the 'correct' direction to minimize the cost function, as in the latest version of the CMB algorithm. Section 4 deals exclusively with this topic, so only the salient points are given here.

Figure 5 shows the $\log(N_W)$ versus D_m variations derived from the ground-based, OceanRain, and airborne DSDs. A few caveats (see Table 1) of the interpretation of this figure are: (a) the varying number of data points in each rainfall regime (locations); (b) the differences in instrument types and measurement volumes and if theoretical drop fall speeds or measured values are used; (c) no classification of rain type is done, e.g., stratiform or convective rain.

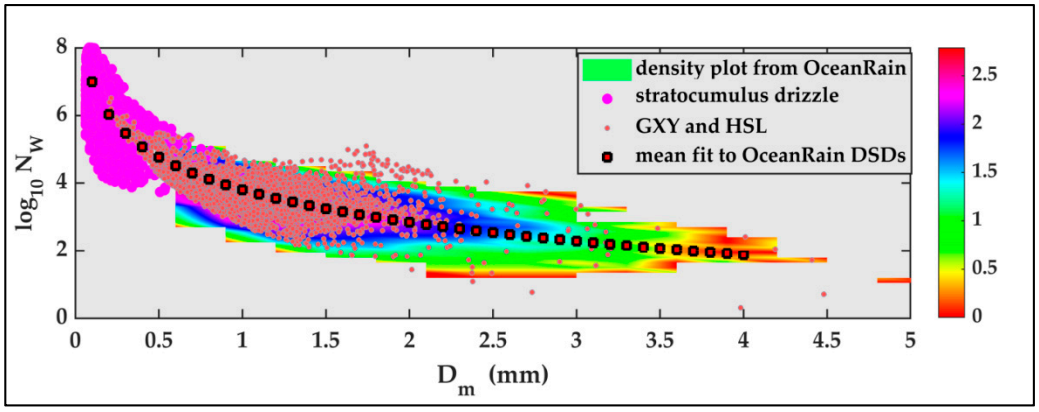

Figure 5. Scatterplot of $\log_{10}$ (N_W) versus D_m from three regimes described in the legend. The contoured density plot (refer to color bar) is from OceanRain. The mean fit to OceanRain is $N_W = 6383.8\ D_m{}^{-3.19}$, where N_W is in $mm^{-1}\ m^{-3}$ shown as red-filled black squares. The GXY- and HSV-based points are shown in light red and those from stratocumulus DSDs are shown in magenta.

In spite of these caveats, the following points can be made:

(a) From the high resolution (25 microns) 'fast' 2D cloud probe aircraft DSD data, we found that the drizzle D_m is generally <0.5 mm with N_W spanning at least two orders of magnitude for any given D_m;

(b) The N_W–D_m points from GXY-HSV appear to smoothly merge with the drizzle data for D_m < 0.35 mm;

(c) The mean power law fit from [22], from their OceanRain DSDs, shown as 'squares', is an excellent fit through the entire size range covered by all datasets (with the exception of drizzle; see Appendix A), despite the large variability of N_W for any given D_m. This is a major finding of this paper.

3.4. The Relationship between Rain Rate and DSD Gamma Parameters

The rain rate (R) variability is not only due to variations in the parameters that describe the parametric form of the DSD but also the intrinsic or 'underlying' DSD shape termed h(x), which arises as a result of the scaling normalization framework [3,4]. If the h(x) is stable across different rain types and climatologies, it forms a strong constraint that can be used in satellite (and ground-based) radar rainfall retrievals. For example, if the parametric form of h(x) is gamma, then a constant shape factor (e.g., μ = 2 to 3) defines h(x), provided the small drop truncation is negligible. If the disdrometer cannot measure the small drop end accurately, the h(x) can be stable but incorrect. In any case, N_W and D_m are the two unknown DSD parameters that need to be retrieved. The ideal scenario is the selection of the number and order of the reference moments, whereby the scatter in h(x) is greatly reduced. In practice, the integral quantities that need to be estimated are R and rain water content (W) and perhaps other moments along with their error statistics. The GPM mission has adopted the Testud et al. [1] formulation (i.e., the scaled-normalized form) of the DSD.

From a theoretical (normalized) gamma model with parameters (N_W, D_m, and μ) along with the simplified fall speed relation $v = 3.78\ D^{0.67}$ [37], where v is in ms^{-1} and D in mm, it follows from [1] that:

$$\frac{R}{N_W} = 3.78\left[0.6\pi * 10^{-3}\right]\frac{6}{4^4}\frac{(4+\mu)^{(\mu+4)}}{\Gamma(4+\mu)}\Gamma(\mu+4.67)\frac{[\Gamma(\mu+4)]^{(\mu+4.67)}}{\Gamma(\mu+5)^{(\mu+4.67)}}D_m{}^{4.67} \quad (1)$$

$$\frac{R}{N_W} = \alpha D_m{}^{4.67} \quad (2)$$

Figure 6 shows the theoretical plot of α = f(μ), showing that α varies very slowly with μ in the range of −2 to 10. Figure 7 shows the variation in R/N_W versus D_m obtained by

(a) simulating a gamma distribution with the parameters being uncorrelated from each other but uniformly distributed in the intervals 200 to 6×10^6 mm^{-1} m^{-3}, 0 to 4 mm, and -2 to 4 for N_W, D_m, and μ, respectively, and (b) using the theoretical equation with $\mu = 0$, i.e., exponential DSD. The agreement between using (a) random gamma (i.e., with random parameters being uniform in their respective intervals) and (b) a fixed gamma with shape parameter 0 is a point to be noted. To the best of our knowledge, this point has not been made in the literature. A simple explanation is that N_W cancels off in the ratio R/N_W. The residual variability in R/N_W is then due to (μ, D_m). However, in the random gamma simulations, there is no imposed correlation between $\log(N_W)$ and D_m or R and D_m. To complete this sub-section, Figure 8 compares R/N_W versus D_m from the measured DSDs from the 1-s marine stratocumulus, OceanRain, and GXY-HSV. The curves are practically identical, with differences in R/N_W being of the order of <1% in log scale.

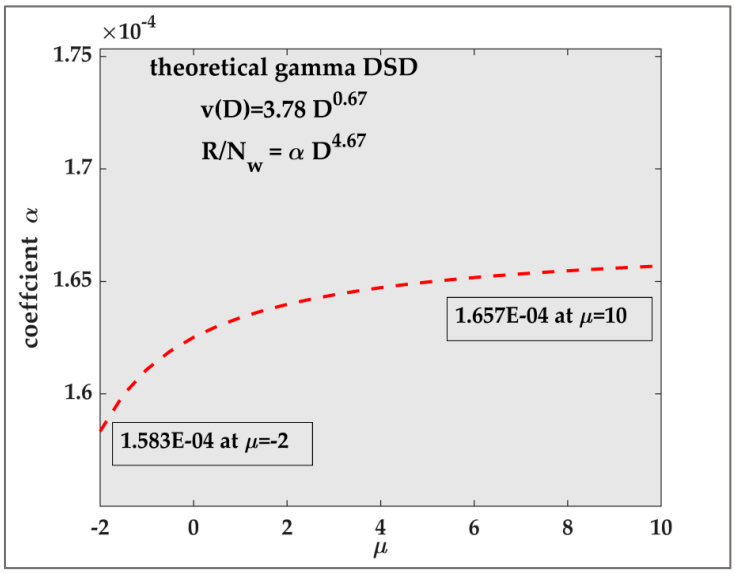

Figure 6. The coefficient α versus shape factor μ for a theoretical gamma with fall speed power law v(D) in m s^{-1}, D in mm, R in mm h^{-1}, and N_W in mm^{-1} m^{-3}. Values of α are given within textboxes for $\mu = -2$ and $\mu = 10$.

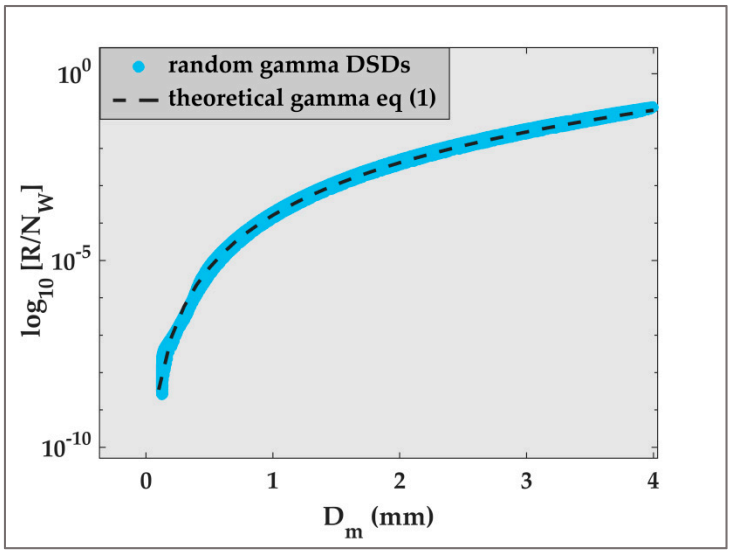

Figure 7. Rain rate (in mm h^{-1}) normalized by N_W (in mm^{-1} m^{-3}) versus D_m (in mm). We compare random gamma DSDs with the theoretical result in Equation (1) with $\mu = 0$.

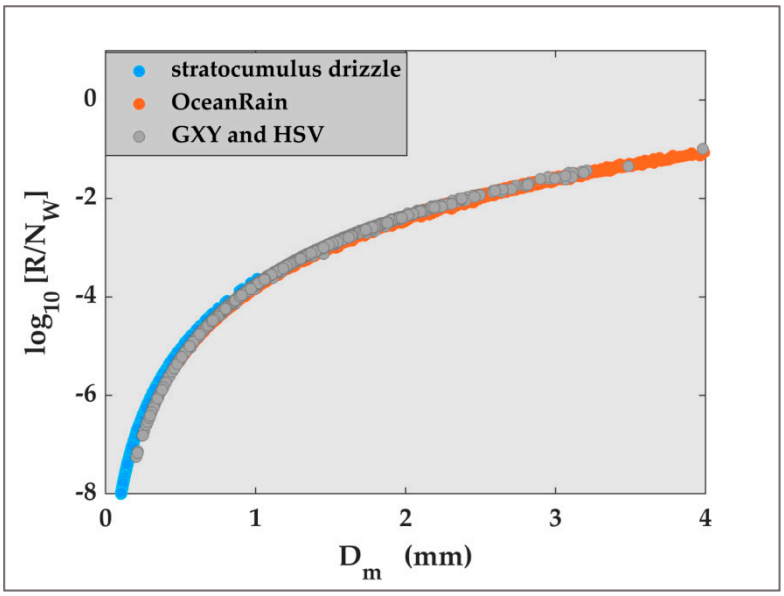

Figure 8. As in Figure 7, except DSDs from stratocumulus drizzle, OceanRain, and GXY-HSV.

3.5. The Relation between Normalized Radar Quantities and D_m

The CMB algorithm uses measured Z_{ku} and the generalized Hitschfeld–Bordan algorithm [19], where the specific attenuation k_{ku} versus Z_{ku} relation is expressed as a power law, to derive the initial profile of D_m. In this context, Figure 9 is important as the DSD-based simulations of k_{ku} and Z_{ku} (using the T-matrix scattering code; [38]) and their ratio (from various regimes described in the legend) fall on an 'invariant' curve without the need for rain type classification. Note that we have added DSDs from the outer rain bands of tropical storms Nate and Irma (after landfall near Huntsville) and hurricane Dorian (as it traversed over Wallops [34,35]). These DSDs are primarily stratiform with bright-band and some embedded weak convection (in total covering > 25 h of rainfall), with Nate having the lowest R (shallow and warm rain at times). For $0.5 < D_m < 2.5$ mm, their overlap with OceanRain and GXY-HSV is visually excellent. The most relevant is the excellent fit of the CMB look-up table values to the measured DSDs (black dashed line). The variability of k_{ku}/Z_{ku} for a given D_m is due to the numerator and denominator being proportional to different moments of the DSD (approximately M_3 and M_6).

We now turn our attention to the relation between R and radar observables, such as Z_{ku}, that have both been normalized by N_W. This relation is used in the CMB retrieval algorithm, and therefore, it is important to compare the lookup tables used in the CMB with measured DSDs and our T-matrix scattering calculations. The lookup tables are based on theoretical gamma DSDs with the parameters D_m and μ being varied systematically (and N_W set to 1 mm^{-1} m^{-3}).

Figure 10 shows the relation between R/N_W and Z_{ku}/N_W for the different regimes. The straight line fits are remarkably parallel to each other. Note that a straight line fit to $\log(R/N_W)$ versus $\log[Z_{ku}/N_W]$ gives the slope (β) and intercept (α) of a power law of the form $R = \alpha N_W^{(1-\beta)} Z_{ku}^{\beta}$. It certainly appears that a single relation, with mean $\alpha = 0.0014$ and mean $\beta = 0.6514$, would be appropriate for all the DSDs considered. Table 2 lists the (α, β) values, including the values for the random gamma simulated DSDs. It can be shown that there is a close relationship between N_W and the parameter ε described by Iguchi et al. [39].

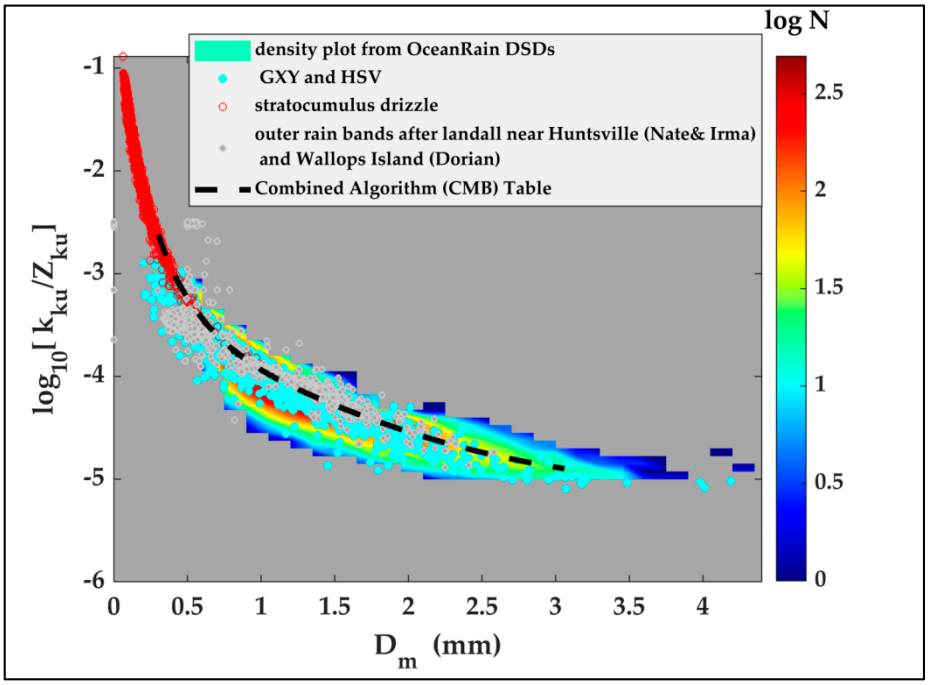

Figure 9. Ku-band-specific attenuation (k_{ku} in dB km^{-1}) normalized by Ku-band reflectivity (Z_{ku} in mm^6 m^{-3}) versus D_m (in mm), from OceanRain DSDs, GXY-HSV DSDs, DSDs from the outer bands of Tropical Storm Irma and Tropical Depression Nate, as well as category-1 Hurricane Dorian, compared with those from the combined algorithm (CMB).

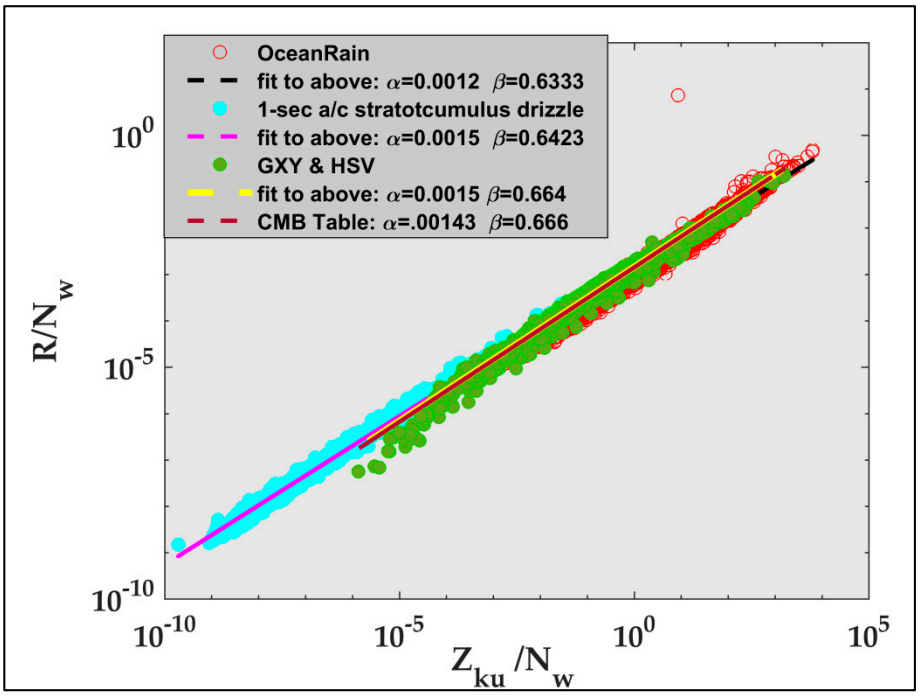

Figure 10. Variation of the rain rate (R in mm h^{-1}) normalized by N_W (in mm^{-1} m^{-3}) versus Ku-band reflectivity (Z_{ku}, in mm^6 m^{-3}). See legend, which lists the regimes.

Table 2. Fitted coefficient α and the exponent β, corresponding to Figures 10 and 11.

DSD Source	Figure 10: $R = \alpha N_W^{(1-\beta)} Z_{ku}^{\beta}$		Figure 11: $R = \alpha N_W^{(1-\beta)} Z_{ka}^{\beta}$	
Stratocumulus drizzle	α = 0.0015	β = 0.6423	α = 0.0014	β = 0.6412
OceanRain	α = 0.0012	β = 0.633	α = 0.0017	β = 0.7339
GXY-HSV	α = 0.0015	β = 0.664	α = 0.0018	β = 0.7336
CMB Table	α = 0.00143	β = 0.666	α =0.00219	β = 0.727

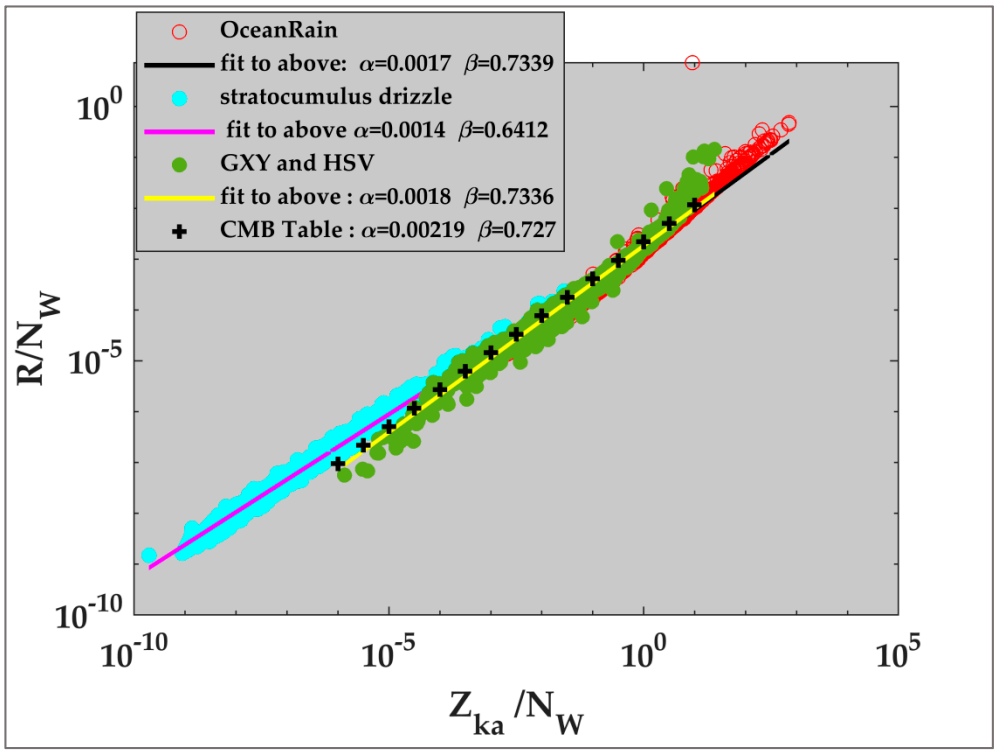

Figure 11. As in Figure 10, but for Ka-band.

At Ka-band, shown in Figure 11, the relationship of normalized R with normalized Z_{ka} is bound to be affected by non-Rayleigh scattering, as indicated by the enhanced scatter for the OceanRain DSDs. Both the GXY-HSV and OceanRain show non-linear behavior in the log-log domain. The slopes vary depending on the DSD source, the stratocumulus drizzle showing the smallest β = 0.64, whereas the GXY-HSV, the random gamma, and the CMB table show that the corresponding β values are very close to 0.73. The CMB fit at Ka-band matches the observations in terms of the slope up to $Ze/N_W \sim 1$, but a more complex piecewise fitting would be required to better match the non-linearity caused by non-Rayleigh scattering.

Another important plot in the context of evaluating the current assumptions held in the CMB algorithm is k/N_W vs. Z_e/N_W (see Figures 12 and 13), which, if linear in the log-log domain, will result in (as before) $k = \alpha N_W^{(1-\beta)} Z_e^{\beta}$. The linearity between the various measured DSDs is not expected to be perfect, i.e., some non-linearity is to be expected at the drizzle end (where different moments are correlated: M_6 versus M_3) and at the upper end (non-Rayleigh scattering versus M_3). This is confirmed in Figure 12 (for Ku-band) and Figure 13 (for Ka-band).

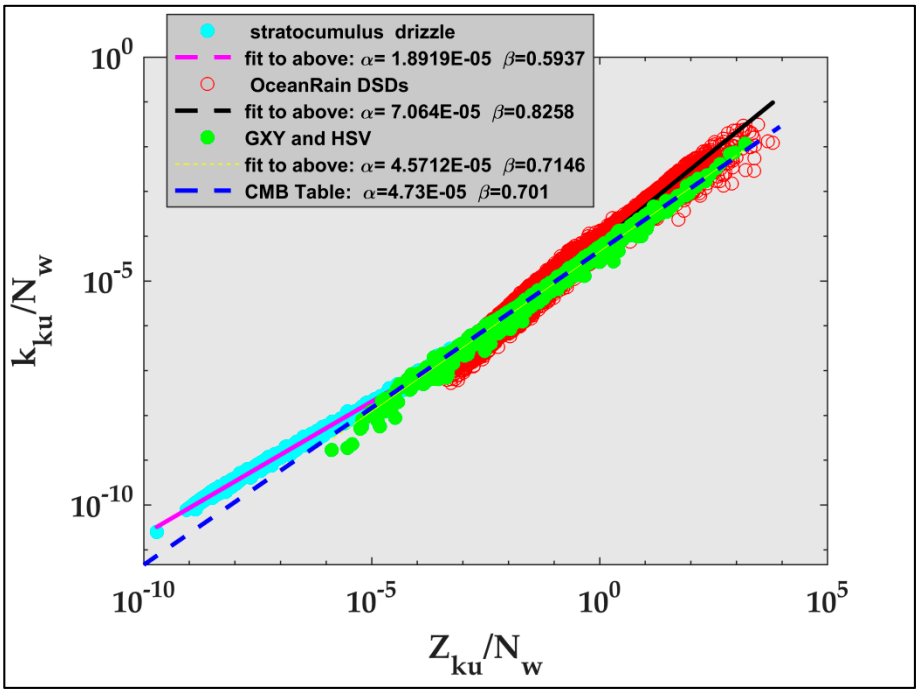

Figure 12. Variation of Ku-band specific attenuation (k_{ku} in dB km^{-1}) normalized by N_W (mm^{-1} m^{-3}) versus Ku-band reflectivity (Z_{ku}, in mm^6 m^{-3}) normalized by N_W. See legend, which lists the regimes.

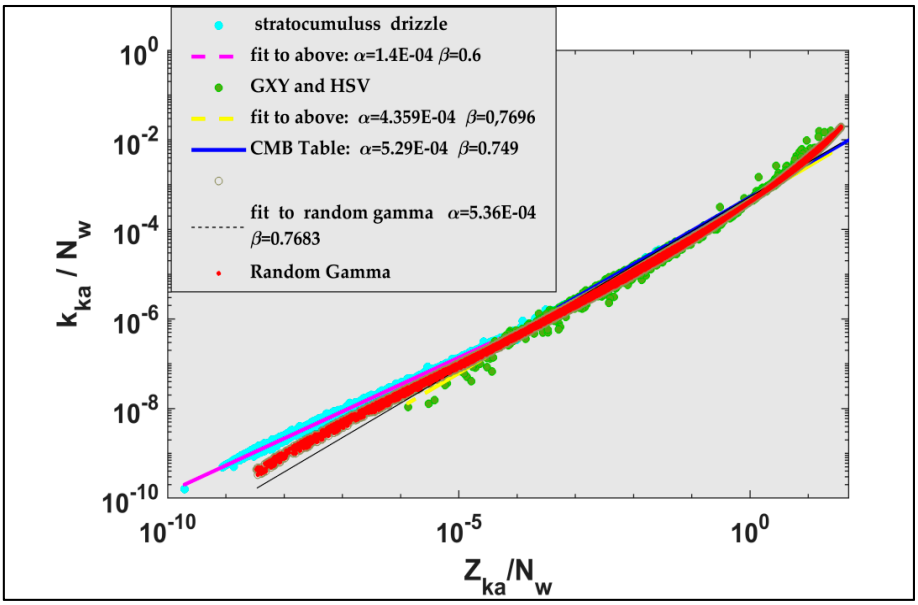

Figure 13. As in Figure 12 but for Ka-band.

Tables 2 and 3 give the coefficient α and the exponent β for the four DSD regimes, as represented by the three datasets. The CMB table values are close to the others, except for the drizzle fits. Additionally, note that the non-linearity is more evident at Ku-band (Figure 12) relative to Ka-band (Figure 13). Atlas et al. [37] showed that at Ka-band, the specific attenuation is linear with rain rate but not at lower frequencies, which would account for the non-linearity at Ku-band. The 'best' match at Ku-band is between the measured DSDs from GXY-HSV and the CMB table. From the radar profiling perspective, normalized k–Z_e relationships are crucial for attenuation correction. The CMB lookup

tables are based on a set of theoretical gamma DSDs (and not measured DSDs), yet the slope and exponent from the CMB tables are in good agreement with measured DSDs (exceptions noted above). Note also from Table 3, that the fit to random gamma-simulated DSDs is nearly identical with the CMB lookup table values.

Table 3. Fitted coefficient α and the exponent β, corresponding to Figures 12 and 13.

DSD Source	Figure 12: $k_{Ku} = \alpha N_W^{(1-\beta)} Z_{Ku}^{\beta}$		Figure 13: $k_{Ka} = \alpha N_W^{(1-\beta)} Z_{Ka}^{\beta}$	
Stratocumulus drizzle	$\alpha = 1.89 \times 10^{-5}$	$\beta = 0.5937$	$\alpha = 1.4 \times 10^{-4}$	$\beta = 0.6$
OceanRain	$\alpha = 7.064 \times 10^{-5}$	$\beta = 0.8258$	$\alpha = 7.0 \times 10^{-4}$	$\beta = 0.715$
GXY-HSV	$\alpha = 4.57 \times 10^{-5}$	$\beta = 0.7146$	$\alpha = 4.36 \times 10^{-4}$	$\beta = 0.769$
CMB Table	$\alpha = 4.73 \times 10^{-5}$	$\beta = 0.701$	$\alpha = 5.29 \times 10^{-4}$	$\beta = 0.749$
Random Gamma	$\alpha = 4.55 \times 10^{-5}$	$\beta = 0.721$	$\alpha = 5.36 \times 10^{-4}$	$\beta = 0.768$

The non-linearity of k/N_W versus Z_e/N_W, while introducing complications in the attenuation correction algorithm, does not fundamentally change the methodology. A major source of uncertainty in the attenuation correction process is obviously N_W. The large variability of N_W and the N_W–D_m relationships in the same (or different) climate regimes was documented in the prior section for our datasets, but these are still limited and need to be expanded to reduce uncertainties. The first results of using the research version of the CMB algorithm seem to indicate that over the Southern Ocean, the CMB algorithm starts the retrieval process with an underestimated value of N_W. This could potentially explain the large discrepancies reported between different satellite products at high southern hemisphere latitudes [17].

From the plots in Figures 10–13, a strong result, hitherto not reported in the literature, is that after normalization, the CMB tables are in very good agreement with observational data and rather surprisingly with random gamma DSDs as well. The marine drizzle DSDs cannot be detected by GPM sensors due to sensitivity limits at Ku- and Ka-bands. Furthermore, the biases and uncertainties in CMB retrievals could arise from the incorrect specification of the a priori state and how representative it is of the climatology of the retrieval regime. One useable constraint is the relation between $\log(N_W)$ and D_m (see Figure 5), which on average is close to the fit from the OceanRain DSDs alone [22,23]. Notwithstanding the large spread due to different rain regimes, we have indirect evidence that N_W–D_m constraints are useful, but not fully proven as of yet, in improving the retrieval of the rain rate using the CMB Algorithm.

4. Application to the CMB Algorithm

As mentioned in the previous sections, the combined algorithm employs a nudging procedure to weakly enforce N_W–D_m climatological constraints in the retrievals. The reason why N_W–D_m climatological relationships are useful is that even when dual-frequency observations are available (i.e., within the matched swath before June 2018 and across the entire swath after the change in the DPR pattern scanning strategy), N_W and D_m cannot be uniquely and unambiguously estimated. Climatological N_W–D_m information improves the estimation process by eliminating estimates inconsistent with a priori observations. The N_W–D_m constraining procedure was introduced in Version 6 of the combined algorithm [25]. Specifically, the relation between N_W and D_m was derived from the GPM Validation Network (VN; [40]) polarimetric radar products and implemented in the algorithm in a two-step procedure. In the first step, a radar-only retrieval is performed, assuming a nominal N_W value that is independent of D_m. In the second step, the N_W is nudged towards the value predicted by the VN relations for the D_m derived in step 1. Specifically, N_W is updated by an increment proportional to the difference between the value predicted by the VN relation and its first step value. In V6, the procedure is applied only to stratiform rain and the nudging coefficient is determined through trial and error. The nudging is not

applied to convective precipitation, as the VN N_W–D_m relationships predicts N_W values that tend to result in substantial underestimation of severe convection.

A two-dimensional N_W–D_m histogram (or density plot) derived from one month (August 2018) of V6 data is shown in Figure 14a. The average VN and OceanRain N_W–D_m relationships are also shown in the figure. As apparent in the figure, although the (color contoured) density plot of the retrieved N_W–D_m exhibits an inverse relationship qualitatively similar to those derived from direct observations, there are also significant discrepancies, especially for large D_m values. Some of these discrepancies may be explained by the differences between the spatial scales of the satellite and ground products. However, notable differences exist between the VN and OceanRain fits as well. As the nudging coefficient was determined by trial and error to minimize biases with respect to the same ground reference products as those in [15], the use of the VN-based N_W–D_m relationship (which is highly biased for a small D_m and less biased for a large D_m with respect to the OceanRain relationship) did not result in increased biases for D_m smaller than 0.7 mm and larger than 2.0 mm. This is also the reason the OceanRain fit (which is not used per se in the Nw adjustment) is in better agreement with the density plot of the V6 N_W–D_m data than the VN relationship (which is actually used in the adjustment).

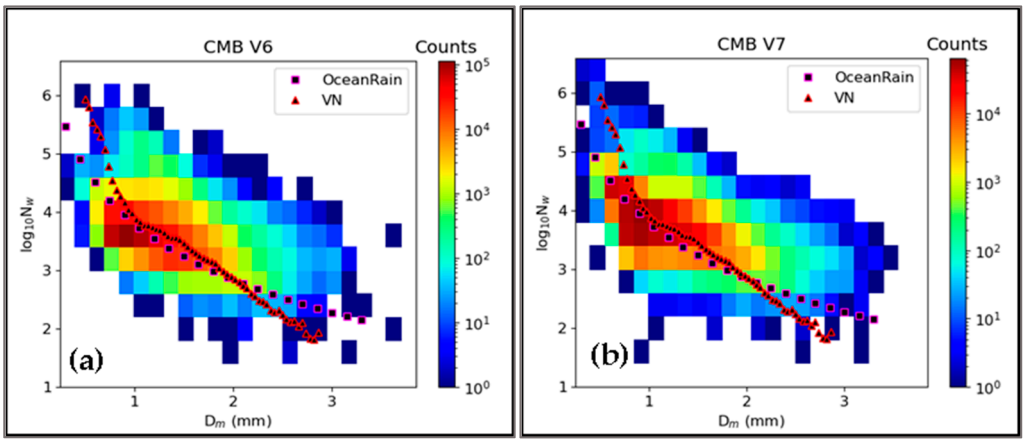

Figure 14. Two-dimensional histogram (or density plot) of joint (N_w, D_m) variables derived using version 6 (V6; panel **a**) and version 7 (V7; panel **b**) of the combined algorithm. Superimposed are the mean N_W–D_m derived from the Validation Network (VN) and used to constrain the retrievals in V6 and V7 (symbolized with triangles) and the fit to OceanRain N_W–D_m data (symbolized with squares).

As the details of this research were still emerging at the time the N_W–D_m nudging procedure was revisited in V7 of the combined algorithm, the VN N_W–D_m rather than OceanRain curve (which is also consistent with the GXY-HSV dataset) was used. Nevertheless, several changes were introduced in the algorithm. Specifically, the nudging procedure was extended to convective precipitation as well. As the VN stratification by precipitation types did not result in significantly different N_W–D_m curves (except for very large D_m), the same curve shape was used for both convective and stratiform. However, the convective curve was shifted upwards by $\log_{10}(N_W) = 0.5$ relative to the stratiform curve. That is, N_W was nudged towards a relationship that predicts a value of $\log_{10}(N_W)$ that is larger by 0.5 than the curve shown in Figure 14 (which is valid only for stratiform precipitation). The shift was determined by trial and error and evaluation against ground estimates. In retrospect, the OceanRain N_W–D_m curve (which, as mentioned before, is consistent with the GXY-HSV dataset) is a better option, but other items requiring attention in the combined algorithm (such as the mitigation of ground clutter and uncertainties in orographic) precluded additional N_W–D_m updates in V7. Nevertheless, the current N_W–D_m updates resulted in an overall increase of 7% of surface rain rates over land, which appear to offset some known biases in V6, and better consistency between single and dual frequency retrievals. The V7 histogram (density plot) of retrieved N_W and D_m is shown

in Figure 14b. As apparent in the figure, the agreement between the combined retrievals and OceanRain is improved for the same reason mentioned in the previous paragraph. The most significant changes in the V7 N_W–D_m two-dimensional histogram (density plot) relative to the V6 density plot appear to occur for D_m values around 1.0 mm and smaller. Nevertheless, the discrepancies between retrieved N_W–D_m and the fit to the OceanRain data for $D_m > 2.0$ mm are large for both V6 and V7 and are suggestive of Non-Uniform Beam Filling (NUBF) effects that may impact both the combined retrievals and the OceanRain analysis. The reconciliation of these discrepancies is left to future studies, as it likely requires a systematic revision of the NUBF parameterizations in the combined algorithm and an extended methodology to mimic NUBF effects in the N_W–D_m relation derived from the OceanRain data.

5. Discussion and Summary

Multiple studies [41,42], have shown that dual frequency space-borne radar observations are generally insufficient to unambiguously estimate rain DSDs. The inclusion of Path Integrated Attenuation (PIA) estimates from the Surface Reference Technique (SRT; [43]) improves the accuracy of N_W and D_m estimates [44], but the SRT PIA estimates are not always reliable and usable in the estimation process. Similarly, the inclusion of over-ocean radiometer observations in the estimation process, although beneficial [45], does not fully address the ambiguity problem, as in some situations, the signal from the surface and cloud water cannot be reliably separated from that of rain in the radiometer observations. As a consequence, additional information, such as the inverse climatological relation between N_W and D_m, is necessary to further improve the accuracy of precipitation estimates from space-borne radar observations.

Jointly, the four DSD datasets investigated in this study span a large range of normalized intercepts N_W and mass-weighted mean diameters D_m. However, a unifying mean N_W–D_m relation appears to exist. Specifically, a relationship between N_W and D_m was derived exclusively from the OceanRain dataset. At the same time, the joint N_W–D_m distributions from the OceanRain and the GXY-HSV datasets overlap significantly, which, consequently, makes the OceanRain N_W–D_m relationship a good fit for the GXY-HSV dataset as well. This suggests that the OceanRain N_W–D_m relationship would be an appropriate constraint for global space-borne radar-based precipitation algorithms, such as the GPM combined algorithm. A comparison between the operational N_W–D_m relation used as a constraint in versions 6 and 7 of the combined algorithm and the OceanRain relation shows deficiencies in the combined relation for small drops ($D_m < 1$ mm) and large drops ($D_m > 2$ mm). However, given that the constraining procedure involves nudging coefficients that have been determined by trial and error and validated against ground precipitation products, the impact of inadequacies in the combined N_W–D_m constraint is rather limited. Nevertheless, the implementation of the OceanRain relation in the combined algorithm is likely to result in more accurate precipitation estimates and a better agreement between the N_W–D_m distributions estimated by the combined algorithm and the N_W–D_m distributions from the three datasets investigated in this study. Other priorities in the combined algorithm, such as the mitigation of ground clutter effects, precluded the implementation of the OceanRain relation in version 7 of the combined algorithm, but it is anticipated that the OceanRain N_W–D_m will be implemented in the next version of the combined algorithm.

We have devoted considerable effort to comparing the statistical relationships between the parameters of the measured gamma DSD distributions, such as N_W–D_m, R/N_W versus D_m, and k_{ku}/Z_{ku} versus D_m. These statistical relationships are in excellent agreement with the mean fit from other similar studies [27,29]. Figures 10–13 showed important normalized relationships between specific attenuation and reflectivity, and R/N_W versus k/Z_e, which were compared to the equivalent relationships in the CMB lookup tables. Although this study has demonstrated that some improvements could be brought to the ka-band relationships to better account for non-Rayleigh scattering, the overall agreement

between CMB lookup tables and the simulations from measured DSDs was excellent in terms of mean power law fit values as compared in Tables 2 and 3. This suggests that the combined lookup tables [15] are not a major source of uncertainty in the combined estimates, which is an important finding of this paper (which we believe has not been reported in other studies). It appears that the limited and hard to untangle amount of information in the observations along with other sources of uncertainties such as multiple scattering and non-uniform beam filling effects are the main causes of random and systematic errors in the combined precipitation estimates.

Author Contributions: Conceptualization, V.B. and M.G.; Methodology, Investigation, and Formal Analysis, V.B., M.G., A.P., and M.T.; Data Curation, C.K. and A.P.; Writing—Original Draft Preparation, V.B. and M.G.; Writing—Review and Editing, V.B., M.G., M.T., and A.P.; Supervision, V.B. All authors have read and agreed to the published version of the manuscript.

Funding: V.B. and M.T. were funded by the NASA Atmospheric Dynamics program via Grant Award Number 80NSSC20K0893. M.G. was supported by the NASA Precipitation Measurement Mission program via grant 80NSSC19K0674.

Data Availability Statement: Data can be made available upon request to any of the authors.

Acknowledgments: We wish to thank J. Vivekanandan and J. Jensen from NCAR for supplying quality-controlled aircraft-installed 2D-C 1-s data and G-J Huang for assistance with data processing of the aircraft data.

Conflicts of Interest: The authors declare no conflict of interest. The funders had no role in the design of this study; in the collection, analyses, or interpretation of its data; in the writing of this manuscript, and in the decision to publish these results.

Appendix A. N_W versus D_m Fitted Curve

Figure 5 shows that the power-law fit from [22] was a good overall representation of the variation of N_W with D_m for all datasets for the entire range, despite the large spread, e.g., in N_W for any given D_m. To quantify this spread, we consider here the differences between the N_W from the DSDs and from the power law fit in [22] using logarithmic transformation. If we denote N_W and D_m from the DSDs as $N_W{}^{(measured)}$ and $D_m{}^{(measured)}$, then:

$$\Delta \log_{10} N_W = \log_{10} N_W^{measured} - \log_{10} N_W^{fit} \quad (A1)$$

where:

$$N_W^{fit} = 6383.8 \left(D_m^{measured} \right)^{-3.19} \quad (A2)$$

Histograms of $\Delta \log_{10} N_W$ for the GXY-HSV dataset and the OceanRain dataset are shown in panel (a) of Figure A1, in green and red, respectively. Since the two histograms resemble a Gaussian-like distribution, a non-linear least-squares fit to a function with four unknown parameters, p_0, p_1, p_2, and p_3, was computed for each of the histograms. The function, denoted as f(x), used here is the following:

$$f(x) = p_0 e^{\frac{-v^2}{2}} + p_3 \quad (A3)$$

where:

$$v = \frac{x - p_1}{p_2} \quad (A4)$$

In Equations (A3) and (A4), p_0 will represent the maximum fitted value of the histograms, p_1 the mode (position) of the histograms, p_2 the standard deviation, and p_3 any offsets connected with the histograms. Values of the fitted parameters are given in Table A1.

The fitted curve for the OceanRain Data shows somewhat lower value for p_2 (i.e., narrower) and higher value for p_0 (taller) than for the GXY-HSV; furthermore, it has an offset p_3 very close to zero. This is to be expected since the power-law fit given in Equation

(A2) was originally done for the OceanRain datasets. Both have a p_1 close to zero, indicating that there is very little systematic bias. The overall conclusion here is that Equation (A2) is an excellent representation for the mean variation for both datasets, but that the GXY-HSV curve shows more spread. Note that the N_W versus D_m also has a dependence on rain type, as shown for example in [46], where stratiform and convective rain were shown to be separated by a clear demarcation line. Hence, one can expect further improvement if the two rain types are considered separately.

For the drizzle dataset, however, it was found that Equation (A2) was not a good representation of the N_W–D_m variation; the blue curves in panel (b) of Figure A1 show this clearly. A very clear bias is seen, having the mode of $\Delta \log_{10} N_W$ at ~−0.85.

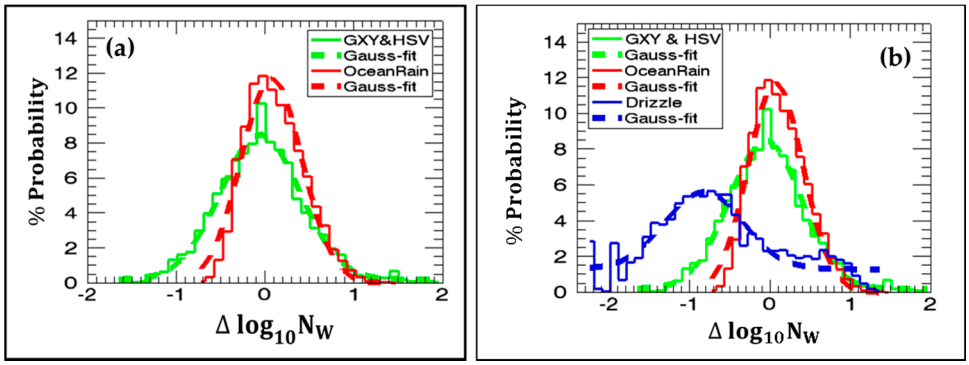

Figure A1. (**a**) Histograms of $\Delta \log_{10} N_W$ for the GXY-HSV (green) and OceanRain (rain) datasets, and their fitted curves; (**b**) the same as (**a**) but with drizzle histograms included (blue).

Table A1. Values of the parameters fitted to the histograms in Figure A1a.

Fitted Parameters	Fitted Values for GXY-HSV Dataset	Fitted Values for OceanRain Dataset
p_0	8.3	11.8
p_1	−0.06	0.07
p_2	0.446	0.342
p_3	0.194	−0.007

References

1. Testud, J.; Oury, S.; Black, R.A.; Amayenc, P.; Dou, X. The concept of "normalized"distribution to describe raindrop spectra: A tool for cloud physics and cloud remote sensing. *J. Appl. Meteorol.* **2001**, *40*, 1118–1140. [CrossRef]
2. Bringi, V.N.; Huang, G.; Chandrasekar, V.; Gorgucci, E. A methodology for estimating the parameters of a gamma raindrop size distribution model from polarimetric radar data: Application to a squall-line event from the TRMM/Brazil campaign. *J. Atmos. Ocean. Technol.* **2002**, *19*, 633–645. [CrossRef]
3. Lee, G.; Zawadzki, I.; Szyrmer, W.; Sempere-Torres, D.; Uijlenhoet, R. A general approach to double-moment normalization of drop size distributions. *J. Appl. Meteorol.* **2004**, *43*, 264–281. [CrossRef]
4. Morrison, H.; Kumjian, M.R.; Martinkus, C.P.; Prat, O.P.; Van Lier-Walqui, M. A general *N*-moment normalization method for deriving raindrop size distribution scaling relationships. *J. Appl. Meteorol. Climatol.* **2019**, *58*, 247–267. [CrossRef]
5. Ulbrich, C.W. Natural variations in the analytical form of the raindrop size distribution. *J. Clim. Appl. Meteorol.* **1983**, *22*, 1764–1775. [CrossRef]
6. Baumgardner, D.; Kok, G.; Dawson, W.; O'Connor, D.; Newton, R. A new ground-based precipitation spectrometer: The Meteorological Particle Sensor (MPS). In Proceedings of the 11th Conference on Cloud Physics, Ogden, UT, USA, 2–3 June 2002; Paper 8.6.
7. Schoenhuber, M.; Lammer, G.; Randeu, W.L. One decade of imaging precipitation measurement by 2D-video-distrometer. *Adv. Geosci.* **2007**, *10*, 85–90. [CrossRef]
8. Schönhuber, M.; Lammer, G.; Randeu, W.L. The 2D-Video-Distrometer. In *Precipitation: Advances in Measurement, Estimation and Prediction*; Michaelides, S., Ed.; Springer: Berlin/Heidelberg, Germany, 2008; pp. 3–31; ISBN 978-3-540-77654-3.

9. Thurai, M.; Bringi, V.N. Application of the generalized gamma model to represent the full rain drop size distribution spectra. *J. Appl. Meteorol. Climatol.* **2018**, *57*, 1197–1210. [CrossRef]
10. Thurai, M.; Bringi, V.; Gatlin, P.N.; Petersen, W.A.; Wingo, M.T. Measurements and modeling of the full rain drop size distribution. *Atmosphere* **2019**, *10*, 39. [CrossRef]
11. Williams, C.R.; Kruger, A.; Gage, K.S.; Tokay, A.; Cifelli, R.; Krajewski, W.F.; Kummerow, C. Comparison of simultaneous rain drop size distributions estimated from two surface disdromters and a UHF profiler. *Geophys. Res. Lett.* **2000**, *27*, 1763–1766. [CrossRef]
12. Kozu, T.; Iguchi, T.; Shimomai, T.; Kashiwagi, N. Raindrop size distribution modeling from a statistical rain parameter relation and its application to the TRMM precipitation radar rain retrieval algorithm. *J. Appl. Meteorol. Climatol.* **2009**, *48*, 716–724. [CrossRef]
13. Bringi, V.N.; Chandrasekar, V.; Hubbert, J.; Gorgucci, E.; Randeu, W.L.; Schoenhuber, M. Raindrop size distribution in different climatic regimes from disdrometer and dual-polarized radar analysis. *J. Atmos. Sci.* **2003**, *60*, 354–365. [CrossRef]
14. Petersen, W.A.; Kirstetter, P.E.; Wang, J.; Wolff, D.B.; Tokay, A. The GPM Ground Validation Program. In *Satellite Precipitation Measurement*; Springer: Cham, Germany, 2020; pp. 471–502.
15. Grecu, M.; Olson, W.S.; Munchak, S.J.; Ringerud, S.; Liao, L.; Haddad, Z.; Kelley, B.L.; McLaughlin, S.F. The GPM Combined Algorithm. *J. Atmos. Ocean. Technol.* **2016**, *33*, 2225–2245. [CrossRef]
16. Huffman, G.J.; Bolvin, D.T.; Braithwaite, D.; Hsu, K.; Joyce, R.; Xie, P.; Yoo, S.H. NASA global precipitation measurement (GPM) integrated multi-satellite retrievals for GPM (IMERG). In *Algorithm Theoretical Basis Document (ATBD)*; 2019; Version 6; p. 39. Available online: https://gpm.nasa.gov/sites/default/files/document_files/IMERG_ATBD_V06.pdf (accessed on 19 June 2021).
17. Skofronick-Jackson, G.; Petersen, W.A.; Berg, W.; Kidd, C.; Stocker, E.F.; Kirschbaum, D.B.; Kakar, R.; Braun, S.A.; Huffman, G.J.; Iguchi, T.; et al. The Global Precipitation Measurement (GPM) mission for science and society. *Bull. Am. Meteorol. Soc.* **2017**, *98*, 1679–1695. [CrossRef] [PubMed]
18. Kidd, C.; Becker, A.; Huffman, G.J.; Muller, C.L.; Joe, P.; Skofronick-Jackson, G.; Kirschbaum, D.B. So, how much of the earth's surface is covered by rain gauges? *Bull. Am. Meteorol. Soc.* **2017**, *98*, 69–78. [CrossRef]
19. Hitschfeld, W.; Bordan, J. Errors inherent in the radar measurement of rainfall at attenuating wavelengths. *J. Meteorol.* **1954**, *11*, 58–67. [CrossRef]
20. Bringi, V.N.; Tolstoy, L.; Thurai, M.; Petersen, W.A. Estimation of spatial correlation of rain drop size distribution parameters and rain rate using NASA's S-band polarimetric radar and 2D-video disdrometer network: Two case studies from MC3E. *J. Hydrometeor.* **2015**, *16*, 1207–1221. [CrossRef]
21. Viltard, N.; Kummerow, C.; Olson, W.S.; Hong, Y. Combined use of the radar and radiometer of TRMM to estimate the influence of drop size distribution on rain retrievals. *J. Appl. Meteorol.* **2000**, *39*, 2103–2114. [CrossRef]
22. Protat, A.; Klepp, C.; Louf, V.; Petersen, W.A.; Alexander, S.P. The latitudinal variability of oceanic rainfall properties and its implication for satellite retrievals: 1. Drop size distribution properties. *J. Geophys. Res. Atmos.* **2019**, *124*, 13291–13311. [CrossRef]
23. Protat, A.; Klepp, C.; Louf, V.; Petersen, W.A.; Alexander, S.P.; Barros, A.; Leinonen, J.; Mace, G.G. The latitudinal variability of oceanic rainfall properties and its implication for satellite retrievals: 2. The relationships between radar observables and drop size distribution parameters. *J. Geophys. Res. Atmos.* **2019**, *124*, 13312–13324. [CrossRef]
24. Duncan, D.I.; Eriksson, P.; Pfreundschuh, S.; Klepp, C.; Jones, D.C. On the distinctiveness of observed oceanic raindrop distributions. *Atmos. Chem. Phys.* **2019**, *19*, 6969–6984.
25. Olson, W.S.; Masunaga, H.; GPM Combined Radar-Radiometer Algorithm Team. *GPM Combined Radar-Radiometer Precipitation Algorithm Theoretical Basis Document (Version 4)*; NASA: Washington, DC, USA, 2019.
26. Gatlin, P.N.; Petersen, W.A.; Pippitt, J.L.; Berendes, T.A.; Wolff, D.B.; Tokay, A. The GPM validation network and evaluation of satellite-based retrievals of the rain drop size distribution. *Atmosphere* **2020**, *11*, 1010. [CrossRef]
27. Chase, R.J.; Nesbitt, S.W.; McFarquhar, G.M. Evaluation of the Microphysical Assumptions within GPM-DPR Using ground-based observations of rain and snow. *Atmosphere* **2020**, *11*, 619. [CrossRef]
28. Tokay, A.; D'Adderio, L.P.; Wolff, D.B.; Petersen, W.A. Development and evaluation of the raindrop size distribution parameters for the NASA global precipitation measurement mission ground validation program. *J. Atmos. Ocean. Technol.* **2020**, *37*, 115–128. [CrossRef]
29. Liao, L.; Meneghini, R.; Iguchi, T.; Tokay, A. Characteristics of DSD bulk parameters: Implication for radar rain retrieval. *Atmosphere* **2020**, *11*, 670. [CrossRef]
30. Rasmussen, R.; Baker, B.; Kochendorfer, J.; Meyers, T.; Landolt, S.; Fischer, A.P.; Black, J.; Thériault, J.M.; Kucera, P.; Gochis, D.; et al. How well are we measuring snow: The NOAA/FAA/NCAR winter precipitation test bed. *Bull. Am. Meteorol. Soc.* **2012**, *93*, 811–829. [CrossRef]
31. Larsen, M.; Schönhuber, M. Identification and characterization of an anomaly in 2-dimensional video disdrometer data. *Atmosphere* **2018**, *9*, 315. [CrossRef]
32. Wood, R.; Mechoso, C.R.; Bretherton, C.S.; Weller, R.A.; Huebert, B.; Straneo, F.; Albrecht, B.A.; Coe, H.; Allen, G.; Vaughan, G.; et al. The VAMOS Ocean-cloud-atmosphere-land study regional experiment (VOCALS-REx): Goals, platforms, and field operations. *Atmos. Chem. Phys.* **2011**, *11*, 627–654. [CrossRef]
33. Klepp, C.; Michel, S.; Protat, A.; Burdanowitz, J.; Albern, N.; Kähnert, M.; Dahl, A.; Louf, V.; Bakan, S.; Buehler, S.A. OceanRAIN, a new in-situ shipboard global ocean surface-reference dataset of all water cycle components. *Sci. Data* **2018**, *5*, 180122. [CrossRef]

34. Thurai, M.; Bringi, V.N.; Wolff, D.B.; Marks, D.A.; Pabla, C.S. Drop size distribution measurements in outer rainbands of hurricane dorian at the NASA wallops precipitation-research facility. *Atmosphere* **2020**, *11*, 578. [CrossRef]
35. Bringi, V.; Seifert, A.; Wu, W.; Thurai, M.; Huang, G.-J.; Siewert, C. Hurricane dorian outer rain band observations and 1D particle model simulations: A case study. *Atmosphere* **2020**, *11*, 879. [CrossRef]
36. Abel, S.J.; Boutle, I.A. An improved representation of the rain size spectra for single-moment microphysics schemes. *Quart. J. R. Meteorol. Soc.* **2012**, *138*, 2151–2162. [CrossRef]
37. Atlas, D.; Ulbrich, C.W. Path- and area-integrated rainfall measurement by microwave attenuation in the 1–3 cm band. *J. Appl. Meteorol. Climatol.* **1977**, *16*, 1322–1331. [CrossRef]
38. Barber, P.; Yeh, C. Scattering of electromagnetic waves by arbitrarily shaped dielectric bodies. *Appl. Opt.* **1975**, *14*, 2864–2872. [CrossRef]
39. Iguchi, T.; Kozu, T.; Meneghini, R.; Awaka, J.; Okamoto, K. Rain-profiling algorithm for the TRMM precipitation radar. *J. Appl. Meteorol.* **2000**, *39*, 2038–2052. [CrossRef]
40. Schwaller, M.R.; Morris, K.R. A ground validation network for the global precipitation measurement mission. *J. Atmos. Ocean. Technol.* **2011**, *28*, 301–319. [CrossRef]
41. Meneghini, R.; Kozu, T.; Kumagai, H.; Boncyk, W.C. A study of rain estimation methods from space using dual-wavelength radar measurements at near-nadir incidence over ocean. *J. Atmos. Ocean. Technol.* **1992**, *9*, 364–382. [CrossRef]
42. Haddad, Z.S.; Meagher, J.P.; Durden, S.L.; Smith, E.A.; Im, E. Drop size ambiguities in the retrieval of precipitation profiles from dual-frequency radar measurements. *J. Atmos. Sci.* **2006**, *63*, 204–217. [CrossRef]
43. Meneghini, R.; Iguchi, T.; Kozu, T.; Liao, L.; Okamoto, K.; Jones, J.A.; Kwiatkowski, J. Use of the surface reference technique for path attenuation estimates from the TRMM precipitation radar. *J. Appl. Meteorol.* **2000**, *39*, 2053–2070. [CrossRef]
44. Ferreira, F.; Amayenc, P.; Oury, S.; Testud, J. Study and tests of improved rain estimates from the TRMM precipitation radar. *J. Appl. Meteorol.* **2001**, *40*, 1878–1899. [CrossRef]
45. Grecu, M.; Anagnostou, E.N. Use of passive microwave observations in a radar rainfall-profiling algorithm. *J. Appl. Meteorol.* **2002**, *41*, 702–715. [CrossRef]
46. Thurai, M.; Bringi, V.; Wolff, D.; Marks, D.; Pabla, C. Testing the drop-size distribution-based separation of stratiform and convective rain using radar and disdrometer data from a mid-latitude coastal region. *Atmosphere* **2021**, *12*, 392. [CrossRef]